Volume 226 • Number 7 • September 2021

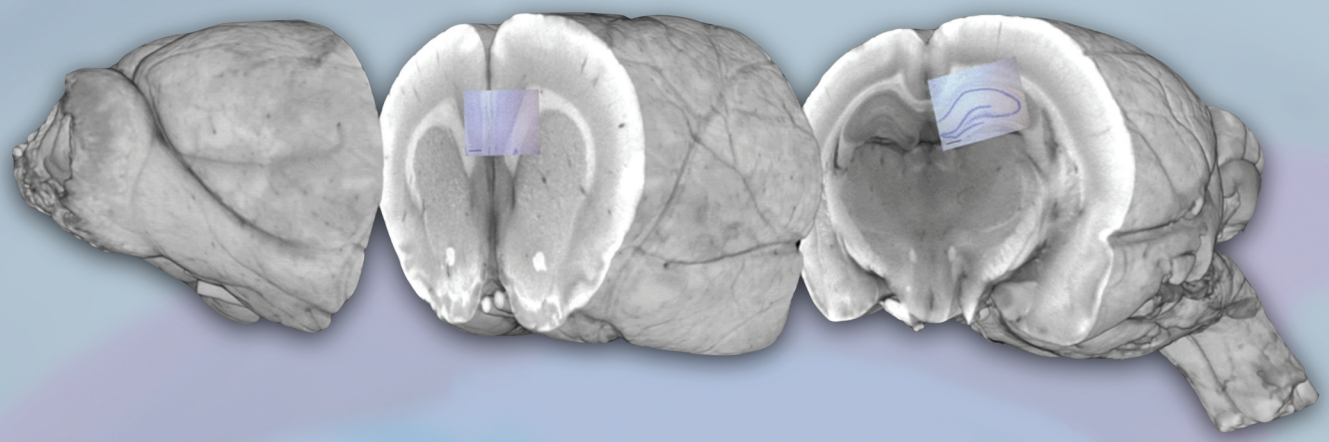

Brain Structure & Function

Springer

Brain Structure and Function (2021) 226:2153–2168
https://doi.org/10.1007/s00429-021-02316-6

ORIGINAL ARTICLE

Multiscale imaging of the rat brain using an integrated diceCT and histology workflow

Paul M. Gignac[1] · Haley D. O'Brien[1] · Jimena Sanchez[2] · Dolores Vazquez-Sanroman[1]

Received: 19 January 2021 / Accepted: 7 June 2021 / Published online: 26 June 2021

Abstract

Advancements in tissue visualization techniques have spurred significant gains in the biomedical sciences by enabling researchers to integrate their datasets across anatomical scales. Of particular import are techniques that enable the interpolation of multiple hierarchical scales in samples taken from the same individuals. In this study, we demonstrate that two-dimensional histology techniques can be employed on neural tissues following three-dimensional diffusible iodine-based contrast-enhanced computed tomography (diceCT) without causing tissue degradation. This represents the first step toward a multiscale pipeline for brain visualization. We studied brains from adolescent male Sprague–Dawley rats, comparing experimental (diceCT-stained then de-stained) to control (without diceCT) brains to examine neural tissues for immunolabeling integrity, compare somata sizes, and distinguish neurons from glial cells within the telencephalon and diencephalon. We hypothesized that if experimental and control samples do not differ significantly in morphological cell analysis, then brain tissues are robust to the chemical, temperature, and radiation environments required for these multiple, successive imaging protocols. Visualizations for experimental brains were first captured via micro-computed tomography scanning of isolated, iodine-infused specimens. Samples were then cleared of iodine, serially sectioned, and prepared again using immunofluorescent, fluorescent, and cresyl violet labeling, followed by imaging with confocal and light microscopy, respectively. Our results show that many neural targets are resilient to diceCT imaging and compatible with downstream histological staining as part of a low-cost, multiscale brain imaging pipeline.

Keywords Immunofluorescence · Fluorescence · Cresyl violet · Iodine · Eosinophilic · Isoelectric

Introduction

Scientific gains in the understanding of biological organization and complexity are closely associated with technological and methodological gains in bio-imaging. Visualization tools widely used in biomedical and clinical imaging, such as light-sheet microscopy (Voie et al. 1993), magnetic resonance imaging (MRI: Jackson and Langham 1968; Lauterbur 1974; Damadian et al. 1976; Hinshaw et al. 1977; μMRI: Smith et al. 1996; Dodd et al. 1999), white matter tractography (diffusion tensor image analysis; Basser et al. 1994; Jellison et al. 2004), X-ray micro-computed tomography (μCT; Hounsfield 1977; Feldkamp et al. 1989; Rüegsegger et al. 1996), and positron emission tomography (Ter-Pogossian et al. 1975; Phelps et al. 1976; Muehllehner et al. 1976; Hawkins et al. 1992; Jones and Townsend 2017), are continuously refined to improve the visualization of gross anatomical, microscopic, and cellular-level structure and function of biological tissues. These methodological enhancements have spurred significant advancement within the biomedical sciences by enabling researchers to integrate datasets across anatomical scales from the low-resolution capture of gross morphology to the fine-resolution capture of subcellular cytoskeletal elements. Synthetic approaches that combine multiple imaging techniques have the potential to maximize single-specimen data extraction that spans hierarchical, logarithmic scales of tissue organization.

Paul M. Gignac and Dolores Vazquez-Sanroman are co-lead authors.

✉ Dolores Vazquez-Sanroman
dolores.vazquez_sanroman@okstate.edu

[1] Department of Anatomy and Cell Biology, Oklahoma State University Center for Health Sciences, Tulsa, OK 74107, USA

[2] Centro de Investigaciones Cerebrales, Universidad Veracruzana, Xalapa, Mexico

Here, we evaluate the efficacy of using diffusible iodine-based contrast-enhanced computed tomography (diceCT; Gignac et al. 2016) as a low-cost foundation for multiscale anatomical imaging integration by combining high-resolution cellular and gross anatomical brain-visualization techniques. Although same-brain, multiscale visualization has been conducted previously by combining MRI with histology (e.g., Ding et al. 2016), the relatively coarse resolution of most readily available MRI equipment limits the spatial accuracy of placing microscopic-scale information from histology into meso- and macroscopic anatomical contexts. µMRI can achieve finer spatial resolutions as high as 25 microns, potentially overcoming this limitation; however, µMRI scans remain cost-prohibitive, time-consuming, and are hampered by specimen size limitations (de Crespigny et al. 2008). Nonetheless, µMRI remains a popular imaging modality because it is non-disruptive to biological macromolecules, including proteins (Smith et al. 1996). We propose the use of diceCT (Gignac et al. 2016), which is commonly employed in organismal biology research, as a novel, inexpensive, and high-resolution ex vivo alternative to µMRI. DiceCT is an X-ray µCT-imaging technique that utilizes iodine [in the form of Lugol's iodine (I_2KI) or alcoholic iodine (I_2E)] as a contrast agent to permit three-dimensional (3D) visualization of tissue-level neuroanatomy at resolutions superior to MRI-based modalities (de Crespigny et al. 2008; Anderson and Maga 2015; Hughes et al. 2016b; Gignac and Kley 2018). Iodine absorbs X-rays and binds preferentially to sugars and fatty tissues, making it excellent for nervous system visualization due to its clear differentiation of myelinated and non-myelinated structures at micron-scale resolution using µCT (Gignac and Kley 2018).

The application of µCT for studying how the brain is organized has lagged behind its use as a diagnostic tool in biomedical studies (Sengle et al. 2013; Hopkins et al. 2015; Karreman et al. 2016; Morales et al. 2016; Shami et al. 2017). However, µCT-scanner technologies and software optimizations are improving at a rapid pace, allowing increasingly faster scans at micro- and nano-scale resolutions (e.g., Pelc 2014). The swift evolution of µCT imaging is now being leveraged to document a broad array of tissue types at various spatial scales, thereby providing a substrate for multi-scale visualization as, or perhaps more, viable than µMRI. For example, diceCT methods achieve simultaneous visualization of hard and soft tissues, such as the skull with its brain and cranial nerves intact (Gignac and Kley 2018). They also include processing steps that are reversible, affording the opportunity for multiscale, fully registered imaging of the same tissues with more traditional histological approaches. Multi-tool and correlative imaging, such as that widely used in pathology for the structural examination of human tissues (McDonald and Hayes 1969; Morales et al. 2016), enables the co-registration of multiscale datasets from the same sample. Multiscale imaging via diceCT, therefore, holds the potential to maximize the amount of neuroanatomical information retrieved from one individual, which is otherwise practically unattainable using single-scale and destructive approaches (Caplan et al. 2011; Burnett et al. 2014).

Recently, diceCT samples have been used successfully in subsequent thin-section histological protocols. These studies have followed a variety of methodologies, including harnessing the iodine already present in the sample from initial contrast-enhancement (Jeffery et al. 2011) or following a dehydration rinse in ethanol with re-staining using either Giemsa (Herdina et al. 2015), thionine (Hughes et al. 2016a), hematoxylin and eosin (Senter-Zapata et al. 2016; Chen et al. 2012; Nasrullah et al. 2018; Gignac et al. 2021), Marius yellow, crystal red, methyl blue, and/or Luxol fast blue solutions (Heimel et al. 2019). Histological results secondary to diceCT appear to have produced clear identification of two-dimensional (2D) muscular, epithelial, connective, and nervous tissues. Collectively, these studies illustrate the potential for multiscale diceCT-to-histology tissue-imaging pipelines. However, no studies have formally tested post-diceCT histology against non-diceCT controls, nor have any reported successful immunocytochemical and immunofluorescence tissue staining, following diceCT.

Brain tissue is particularly delicate, with neural proteins highly susceptible to degradation under non-idealized chemical and/or thermal conditions (Gwóźdź et al. 1970, 1978; Bowler and Tirri 1974; Millan et al. 1979; Gold et al. 1985) when compared to somatic tissues (Burger and Fuhrman 1964). Destructive ex vivo conditions may include formalin fixation, weeks in a salt-rich and aqueous contrast solution (e.g., I_2KI), repeated staining with refreshed solutions, storage at room temperature, exposure to high levels of X-rays, and de-staining with alternating baths of sodium thiosulfate ($Na_2S_2O_3$) and de-ionized water or 70% ethanol—each of which represents a step in diceCT preparation, imaging, and de-staining protocols (Gignac et al. 2016). The long-term resiliency of nervous tissues to such conditions has not been quantified. To directly address the susceptibility of neurons and glial cells to degradation during diceCT preparation and imaging, we compare post-diceCT and control neural tissue samples by (1) evaluating the specificity and integrity of fluorescence, immunofluorescence, and cresyl violet staining methods; (2) analyzing preserved morphologies; and (3) quantifying neural cells in four regions of interest within the telencephalon and diencephalon. We hypothesize that, given the proper conditions, brain tissue can remain robust to the chemical, temperature, and radiation environments required for multiple imaging protocols, and we quantitatively evaluated this hypothesis by comparing diceCT-histology preparations and histology-only controls. To help guide future studies, we also document instances in our

evaluation of these protocols where deviation from certain steps in the process could preclude successful histological staining. Overall, we demonstrate that diceCT is largely non-destructive of neural tissues for most of the specific neural substrates we examined, and our results support the use of diceCT imaging as part of a multiscale brain imaging pipeline (Hughes et al. 2016a).

Methods

Brain sampling

Six adolescent (120–150 g body weight) male Sprague–Dawley rats (Charles River Laboratories, Franklin, MA, USA) were single-housed on a 12/12-h light/dark cycle with ad libitum access to food and water. All rats were deeply anesthetized with an Avertin/xylazine cocktail and perfused transcardially with cold saline solution (0.9% NaCl) followed by cold 4% paraformaldehyde. After perfusion, cervical vertebrae were removed, followed by postcranial musculature and surrounding connective tissue. Dorsal portions of the parietal and temporal skull bones were detached, and the entire occipital bone was excised. Remaining tissues connecting the skull and brain were severed, and all cranial nerves cut at the roots. Once extracted, brains were placed in 4% paraformaldehyde solution and refrigerated (4 °C) for 24 h, followed by a 0.1 M phosphate-buffer saline solution (PBS with 30% sucrose) with refrigeration (4 °C) for 48–96 h, at which point full immersion was observed. Samples from three brains were prepared for diceCT imaging followed by cresyl violet, fluorescence, and immunofluorescence staining. Samples from three additional brains were prepared as histology-only controls.

DiceCT protocols

Staining

Following 24 h of fixation and up to 96 h of sucrose immersion, experimental rat brains ($n = 3$) were submerged into a 3% weight-by-volume (w/v) solution of Lugol's iodine (I_2KI) for 21 days (at room temperature), following protocols outlined in Gignac et al. (2016) and Gignac and Kley (2018). In an aqueous solution, iodine (I_2) and potassium iodide (KI) become triiodide (iodine trimers; I_3^-) and potassium ions (K^+), and iodine trimers bind differentially to the carbohydrates and lipids present in neural tissues. All three samples were fully submerged in iodine solution, placed on an electric rocker, and protected from light for the duration of stain diffusion. Upon completion, specimens were washed in a deionized water bath for two hours to remove unbound, excess staining agent from external surfaces, which further aids in the differentiation of neural tissues during X-ray imaging (Gignac and Kley 2018). Specimens were then sealed in 50 ml polypropylene centrifuge tubes with polyethylene foam and filled with de-ionized water for CT scanning. Foam and centrifuge tubes were chosen as packing material and containers, respectively, for their relatively low density as compared to iodine-stained tissues. Samples were fully submerged in water to prevent desiccation during scanning.

µCT scanning

All specimens were µCT-scanned on a GE phoenix v|tome|x s240 high-resolution micro-focus CT system (General Electric, Fairfield, CT, USA) at the American Museum of Natural History Microscopy and Imaging Facility (New York, NY, USA). Scan parameters were optimized on a specimen-by-specimen basis, guided by the scout X-ray image and accompanying histogram. All scan parameters follow the recommendations of Gignac and Kley (2018). Due to the similarity of each specimen's size, shape, tissue constituency, and staining, all scans were performed within a narrow range of 110–120 kV, 110–120 micro-Amperage, 333 ms exposure timing and using 6× multi-frame averaging on a tungsten target with a 0.1 mm copper filter. All scans were completed in 107 min at 20–25 µm (µm) resolutions (isometric voxels) to demonstrate equivalency to the highest µMRI resolutions currently available. After scanning, µCT data were reconstructed on an HP z800 workstation (Hewlett-Packard, Palo Alto, CA, USA) equipped with VG Studio Max (Volume Graphics GmbH, Heidelberg, Germany) and exported as TIFF stacks. Stacks were imported into Avizo-Lite 2020 (Thermo Fisher Scientific Inc., Waltham, MA) for 3D model building based on contrast differences between white and gray matter structures, as described in Gignac and Kley (2018) (Supplemental Information 1).

Chemical de-staining

Following X-ray imaging, we used a chemical de-staining process to remove iodine from brain tissues. Brains were cut transversely into anterior and posterior portions (parallel to the planned plane of histological section) to increase the surface area available for diffusion of the de-staining agent. Preliminary efforts by our team identified the dividing of brains into anterior and posterior portions in this manner as a vital step to ensure complete removal of the triiodide contrast agent. Without this step, subsequent histological sectioning resulted in shearing, which left the tissues unsuitable for further histological processing. All specimens were chemically de-stained by submersion in a 1% w/v solution of sodium thiosulfate on an electric rocker for 7 days, followed by 3 days of a deionized water bath to remove excess de-staining agent (Gignac et al. 2016). In solution, sodium

thiosulfate reacts with triiodide, reducing it to iodide (I^-) and chemically de-staining soft tissues (Trevorrow and Fashena 1935; Shakhashiri 1983; Kondo et al. 2001). This protocol was undertaken twice in total to ensure that all iodine was chemically unbound from and physically flushed out of samples prior to histological sectioning and re-staining. We recommend visual inspection of tissue slides at the beginning of histological preparation to confirm that samples are de-stained and free of any residual brown to orange coloration.

Histology preparation

Histological control specimens ($n=3$) were treated following protocols previously published (Vazquez-Sanroman et al. 2017). De-stained (i.e., post-diceCT) and control brains were transferred to a PBS-30% sucrose solution for 1 week. In preparation for cryo-sectioning, samples were embedded using Histoprep frozen tissue embedding medium (Thermo Fisher Scientific Inc.) and immersed in liquid nitrogen for 20 s. Consecutive coronal sections, 15 µm in thickness, were obtained using a cryostat on a − 6 °C setup (Ag Protect Leica CM 1860; Leica Camera AG, Wetzlar, Germany) and stored in an antifreeze solution (30% ethylene glycol, 25% glycerol, 30% sucrose in PBS) at − 20 °C. Histoprep and liquid nitrogen immersion were critical for optimizing this tissue-sectioning protocol. In addition, sections thicker than 15 µm tended to disintegrate upon handling, which leaves them unreliable for staining.

Brain regions from the telencephalon and diencephalon were pre-selected for histological analyses based on expected clear anatomical boundaries and identifiable neuronal or glial cell populations. We probed these brain regions for select cell-type-specific markers that distinguish neurons and glial cells. We also tested for differences between control and post-diceCT preparations to determine if diceCT interferes with immunofluorescence, fluorescence, and standard histological stains commonly used to identify neural phenotypes. We used five stains: three immunofluorescent labels [anti-parvalbumin (PV), anti-glial fibrillary antigen protein (GFAP), and anti-DARPP-32], one fluorescent label for DNA [4',6-diamidino-2-phenylindole (DAPI)], as well as a cresyl violet stain for nucleic acid. These were applied as relevant to the medial prefrontal cortex (PV, DAPI, cresyl violet), mammillary nucleus (GFAP, DAPI), dentate gyrus of the hippocampus (PV, DAPI, cresyl violet), and substantia nigra (anti-DARPP-32, DAPI). These targeted antibodies allowed us to characterize phenotypes for calcium-binding proteins, intermediate filaments, nucleic acids, and dopamine-cAMP-regulated phosphoprotein. See Table 1 for a summary of histological preparations.

Fluorescent staining

To qualitatively and quantitatively examine overall cellular morphologies and to ensure the viability of tissues for antibody reactivity, tissue sections containing portions of the medial prefrontal cortex (mPFC), mammillary nucleus (MM), and dentate gyrus of the hippocampus (DG), and substantia nigra (SN) from all experimental and control specimens were prepared for immunofluorescent staining. Freely floating sections were rinsed seven times for 15 min each at room temperature with Triton X-100:1× Tris-PBS (Tris–HCl 10 mM, sodium phosphate buffer 10 mM, 0.9% NaCl, pH 7.4) and incubated at 4 °C with one of the following primary antibodies: (1) mouse monoclonal anti-parvalbumin (PV) antibody (no. 235, Swant Inc., Marly, Switzerland), diluted 1:1000; or (2) mouse monoclonal anti-glial fibrillary antigen protein (GFAP) (no. 3670, Cell Signaling Technology, Danvers, MA, USA), diluted 1:500; or (3) goat polyclonal anti-DARPP-32 [no. sc-271111 (previously no. sc-8483), Santa Cruz Biotechnology, Dallas, TX, USA], diluted 1:200. Incubations were at 4 °C for 24 h in PBS 0.1 M Triton X-100 containing 3% donkey serum (no. sc-2044, Santa Cruz Biotechnology). After rinsing, tissue was protected from light during a two-hour incubation at room temperature with one of the following secondary antibodies with conjugated fluorochromes: (1) an Alexa Fluor 488 donkey anti-mouse secondary antibody-fluorochrome conjugate (no. A32766, Thermo Fisher Scientific Inc.) diluted 1:500; or (2) Alexa Fluor 488 donkey anti-goat (no. 705-545-147, Jackson Labs, Bar Harbor, ME, USA), diluted 1:500; followed by 4′,6-diamidino-2-phenylindole (DAPI) staining for one

Table 1 Significance values for ANOVA and *t* tests of control and post-diceCT samples stained using anti-parvalbumin, anti-GFAP, DAPI, and anti-DARPP-32 with target neural phenotype indicated

Histological prep	Neural phenotype	Significance
Anti-parvalbumin	GABAergic interneurons	mPFC: $p=0.009$*; DG: $p=0.956$
Anti-GFAP	Glial cell intermediate filament proteins	MM: $p=0.00098$*
DAPI	Nucleic acids	mPFC: $p=0.2219$; DG: $p=0.325$
Anti-DARPP-32	Phosphoprotein in D1 receptor neurons	SN: $p=0.1916$

Significance ($\alpha<0.01$; indicated by asterisk) was identified for somata diameter in the mPFC and anti-GFAP densitometry measurements in the MM. Somata diameters in other brain regions, all cell counts, and all other fluorescent intensity comparisons were not significantly different

minute (no. sc-3598, Santa Cruz Biotechnology). Once the fluorescence reaction occurred, sections were mounted using Mowiol 4-88 reagent (475904-100GM, MilliporeSigma, Burlington, MA, USA).

Cresyl violet staining

To qualitatively evaluate the viability of tissues and cellular morphologies for non-fluorescent labeling, cresyl violet staining was performed using sections of the mPFC and DG from post-diceCT brains only. Free-floating sections [inferred Bregma coordinates: DG: (− 5.3 mm); mPFC: (3.20 mm); Paxinos and Watson 2014] were rinsed and then mounted on gelatin-coated slides. Sections were stained for eight minutes in 0.1% cresyl violet (no. 190-M, Sigma-Aldrich Corp., St. Louis, MO, USA), followed by two rinses of distilled water for 30 s each. Sections were subsequently dehydrated in ascending ethanol concentrations (50–100%; one minute each) and cleared in two changes of xylene. Slides were then coverslipped with DPX mounting medium (no. 06522; Sigma-Aldrich Corp.) and photographed at ×4, ×10, ×20, and ×100 magnifications.

Densitometry measurements and cellular metrics

We examined all immunofluorescent-labelled sections for each region of interest (mPFC, MM, DG, SN) using confocal microscopy (Nikon C1 Digital Eclipse Modular Confocal Microscope System; Nikon Corp., Tokyo, Japan). Confocal images were taken in single XY planes, at a resolution of 1024 × 1024, and 100 Hz speed. Laser intensity, gain, and offset were maintained constant for each image acquisition. We confirmed the presence of GABAergic mPFC neurons in post-diceCT and control tissues by the positive staining of PV. Immunoreactivity was abundant in somata, axons, and terminals, and cells had the general appearance of those reported by earlier investigations, including perfused-fixed brains (Alonso et al. 1992).

We described and quantified histological features of interest using ImageJ software (National Institutes of Health, Bethesda, MD, USA). For the densitometry analysis (GFAP fluorescence in the MM), images were transformed from RGB into binary (black and white) to define objects and backgrounds. ImageJ plugins for noise reduction and background subtraction were applied across all images for each condition. We identified the number of cell nuclei and measured somata diameters in mPFC and DG, as well as cell number in MM, using the positive staining of DAPI. We measured somata diameters in the SN using the positive staining of DARPP-32 (Nair-Roberts et al. 2008). We hand-counted cell nuclei from digital images, but for evaluating somata diameters we used an automated process. First, we traced somata boundaries as polygons for digital selection in ImageJ. Perimeter lengths and areas inside each selection were algorithmically evaluated to estimate circularity measurements for elliptical polygons representing the area of each cell body. The average diameter of each ellipsis was calculated as a proxy for cell-body diameter (Helmy and Azim 2012). We took a conservative approach to automating cell-size estimates by eliminating potentially erroneous effects of small somata size. For example, an idealized circle has a circularity measurement value of 1.0 (see Laine et al. 2019). Elongate, elliptical polygons are characterized by circularity measurements nearer to 0.0, which can be incorrectly reported for exceptionally small cells. Therefore, we excluded diameter values for cells with circularity measurements below 0.02 (Laine et al. 2019) as well as for cells with estimated areas below 19 μm^2 (DeCoster 2007). To avoid measuring incomplete cells, we used the "cleaning edges" function in ImageJ, which excludes cell bodies that are only partially present at image edges. For those cells that remained, closely adjacent cells were isolated using "thresholding" and "watershed" functions (Carpenter et al. 2006). Diameter measurements for control and post-diceCT preparations were then compared statistically (see next).

All immunoreactivity analyses were determined in a region of interest of 40,000 μm^2 Results were expressed as region-specific mean values and standard errors of the mean (SEM). Quantitative evaluations of cellular morphologies made using ImageJ software were constructed to accommodate our small, exploratory sample sizes. Densitometry measurements, somata diameter, and nucleus counts for control and post-diceCT specimens were statistically compared using one-way analyses of variance (ANOVAs) with a small-sample-size penalized Type-III sum of squares, as well as equal variance *t* tests. Region-specific cell sizes and nucleus counts between control and post-diceCT groups were expressed as mean values with SEM. Prior to analysis, all pairwise variables were found to have homogenous variance using Levene's test ($0.5151 > p < 0.9992$; see Supplemental Information 2). In all statistical tests, experimental samples were compared to controls with the level of significance set to $\alpha < 0.01$. Select comparisons are visualized using box plots (Figs. 2–5). All statistical comparisons were conducted using base R and the package {*car*, version 3.0–10} (Fox and Weisberg 2019); dataset and R script, with full statistical tables, are available in the Supplemental Information 2.

Medial prefrontal cortex: parvalbumin, DAPI, and cresyl violet staining

For mPFC-containing tissue sections, we quantified PV and DAPI reactivity and compared treatments using a one-way ANOVA. Parvalbumin-immunoreactive neurons in the mPFC have an identifiable structure and are well recognized as a subpopulation of GABAergic interneurons

(Kubota et al. 1994; Gabbott et al. 1997). Therefore, they represent an excellent target phenotype to study any differences in cellular morphologies between post-diceCT and non-diceCT groups. We considered PV-GABAergic neurons to be those cells that expressed PV in the soma and axonal projections (Alonso et al. 1992; Kubota et al. 1994), and we used these to assess somatic diameter, using one-way ANOVAs. Additionally, we estimated the number of nuclei positively stained by DAPI, also for one-way ANOVAs. Finally, to qualitatively evaluate the viability of tissues and cellular morphologies for non-fluorescent labeling, we also stained MM sections with cresyl violet.

Mammillary nucleus: DAPI and glial fibrillary acidic protein staining

We stained MM sections with DAPI to evaluate cell morphology qualitatively as well as labeled sections using a GFAP antibody. We quantified the GFAP-immunoreactivity of astrocytes and compared their densitometry values by treatment using a one-way ANOVA.

Dentate gyrus: cresyl violet, parvalbumin, and DAPI staining

For DG-containing tissue sections, cresyl violet staining was performed in post-diceCT brains only. We aimed to evaluate if tissue was intact under fluorescent staining (cresyl violet) with light microscopy as well as under immunofluorescence with dark backgrounds (PV). Somata sizes for PV-positive neurons between treatments were analyzed using a student's *t* test. Cell nuclei counts for DAPI-positive neurons between treatments were analyzed using a one-way ANOVA.

Substantia nigra: DAPI and DARPP-32 staining

For the SN we stained sections with DAPI to evaluate cell morphology qualitatively. We also used DARPP-32 staining, which is typically high for the SN (Hemmings and Greengard 1986), to quantify and contrast somata sizes between treatments using a *t* test.

Digital reconstruction

Each diceCT brain was digitally rendered into 3D, using AvizoLite software running on a Mac Pro computer (Apple Inc.; Cupertino, CA, USA). The slice tool was used to move through the 3D volume in planar sections to match 2D histology images with 3D diceCT anatomy. Digital images of the histology sections were virtually placed into anatomical position with their complementary diceCT volume by aligning shared, neuroanatomically fixed landmarks present in both images. Anatomical locations of sampled areas were estimated using established rat-brain atlas reference spaces (Paxinos and Watson 2014; Swanson 2018).

Results

DiceCT imaging

DiceCT revealed that soft-tissue traits, even delicate myelinated structures (Gignac and Kley 2018), could be effectively imaged and visualized (Fig. 1). Clear visualization of tissue-level structures relied on several steps to ensure imaging noise was minimized, including a post-staining wash in de-ionized water, moderate X-ray exposure timing during CT scanning, and several-fold multi-frame image averaging in captured X-ray image processing. See Supplemental Information 1 for whole-brain tissue visualization.

Histological phenotypes

Medial prefrontal cortex: cresyl violet, DAPI, and parvalbumin staining

Brightfield light microscopy of cresyl violet-treated post-diceCT sections was sufficient to reveal cytoarchitectural landmarks (Fig. 1d, 2b). Post-diceCT cresyl violet-staining quality in the mPFC was comparable to that of the post-diceCT cresyl violet-stained DG treatments (see below). DAPI staining was used to determine the number of nuclei and to assess gross cell morphology (Fig. 2c, d). DiceCT staining did not alter the number of DAPI-positive neurons per square millimeter in comparison to control brain tissue (one-way ANOVA; $F = 2.09$, $p = 0.2219$) (Fig. 2e), nor did it qualitatively appear to change cell phenotype. Parvalbumin immunoreactivity in mPFC neurons was within previously reported ranges (e.g., Vazquez-Sanroman et al. 2017). Parvalbumin-immunoreactive cells showed a morphologically heterogeneous subpopulation of non-pyramidal interneurons (Gabbot et al. 1997) with PV-positive axons and pericellular basket-like morphologies that enveloped the perikarya of nearby cell bodies (Fig. 2c, d). Nonetheless, PV-immunoreactive cells also showed that the diceCT pipeline significantly reduced somata diameter in the mPFC by ~ 13.6% on average (one-way ANOVA; $F = 22.77$, $p = 0.009$) (Fig. 2f).

Mammillary nucleus: DAPI and glial fibrillary acidic protein staining

Qualitatively, diceCT preparation, imaging, and de-staining did not modify the appearance of DAPI-labeled nuclei. The distribution of GFAP-immunoreactive elements in controls was consistent with previous reports (Rahati et al. 2016; Vazquez-Sanroman et al. 2017). Intensely stained, evenly

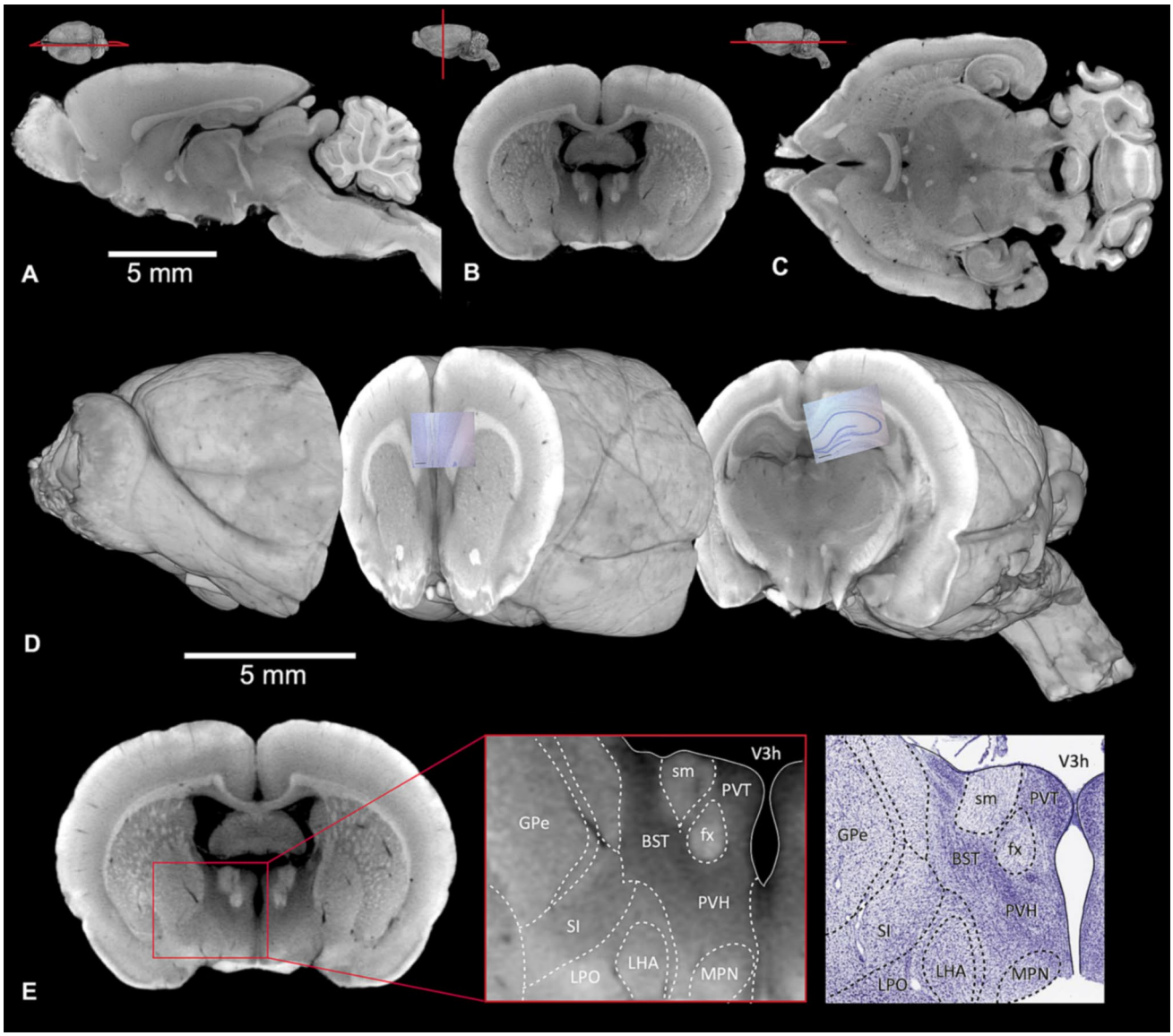

Fig. 1. 2D images of an adolescent rat brain imaged using diceCT in **a** parasagittal, **b**, **e** coronal, and **c** horizontal views alongside a **d** 3D projection that has been digitally dissected to show the mPFC and DG. In **d**, 2D cresyl violet histological images from the mPFC and DG overlay their positions in the 3D model to illustrate the integration of multiscale bio-imaging approaches. **e** Approximate neuroanatomical region assignments within diceCT-processed brain tissue. *AHNa* anterior hypothalamic nucleus, anterior part, *al* ansa lenticularis, *am* anteromedial nucleus thalamus, *ap* area postrema, *BSM* bed nucleus of the stria medullaris (Cajal), *BST* bed nuclei of stria terminalis (Johnston), *dm* dorsomedial nucleus, *fx* column of the fornix, *GPe* globus pallidus, *I* intercalated nuclei of amygdala, *if* interfascicular nucleus raphe, *LHA* lateral hypothalamic area, *LPO* lateral preoptic area, *mg* medial geniculate complex (*v* pars ventralis), *MPN* medial preoptic nucleus (*c* pars centralis, *l* pars lateralis, *m* pars medialis), *MPO* medial preoptic nucleus, *pr* perireuniens nucleus, *pv* paraventricular nucleus, *PVH* paraventricular nucleus hypothalamus, *PVpo* preoptic periventricular nucleus, *PVT* paraventricular nucleus thalamus, *rh* rhomboid thalamic nucleus (Cajal), *SI* substantia innominata (Reil, Reichert), *sm* stria medullaris, and *V3h* third ventricle. Nomenclature following Swanson (2018)

distributed astrocytes with full dendritic body labelling characterized both control and post-diceCT tissues (Fig. 3b, c). However, surface densitometry of cell body and astrocyte processes revealed that diceCT-treated brain tissue decreased GFAP levels compared to controls by ~ 21.3% on average (one-way ANOVA; $F = 74.839$, $p = 0.00098$) (Fig. 3b–d).

Dentate gyrus: cresyl violet, parvalbumin, and DAPI staining

Brightfield light microscopy of cresyl violet-treated experimental sections revealed sufficiently robust staining to delimit specific brain regions and other cytoarchitectural landmarks in the DG. This result indicates both the

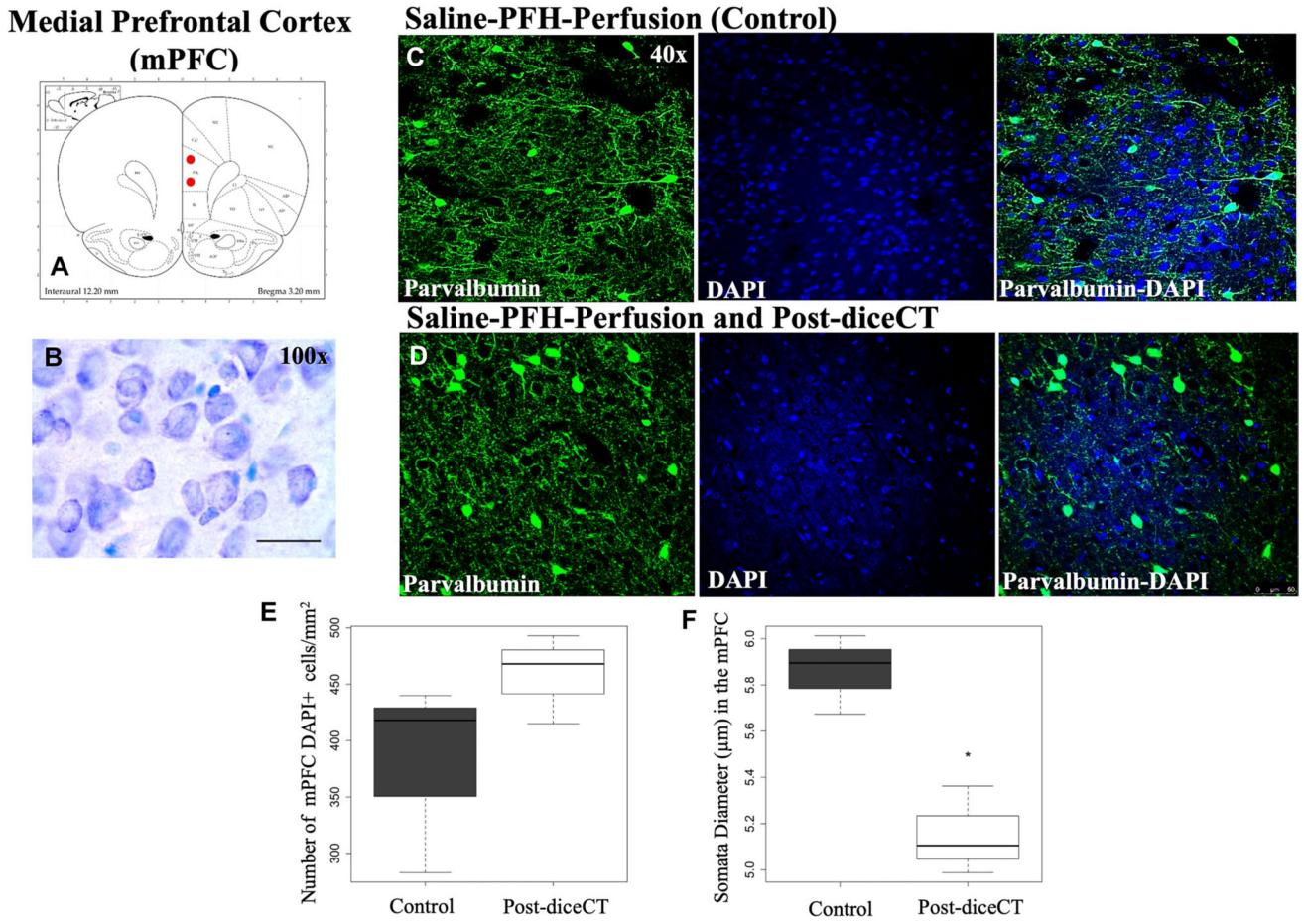

Fig. 2 Medial prefrontal cortex (mPFC) results. **a** Sampled mPFC areas (red) (Paxinos and Watson 2014). **b** Cresyl violet-stained mPFC (scale bar is 20 µm), post-diceCT. **c**, **d** PV immunoreactivity (green), DAPI labeling (blue), and their co-visualization (merge) in mPFC from **c** control and **d** post-diceCT samples; **e** mean (±SEM) number of DAPI-positive cells per mm^2 for control (gray) and post-diceCT (white) mPFC. **f** Mean (±SEM) somata diameter (µm) of DAPI-positive cells for control (gray) and post-diceCT (white) mPFC sections

successful removal of iodine and infiltration of the cresyl violet dye into the cell bodies of the treatment tissues (Fig. 4b–e). Cresyl violet-stained cells from post-diceCT treatments were not structurally aberrant from previous reports (Rekha et al. 2009). Experimental tissues, therefore, showed preserved cell morphology and tissue integrity at high-power magnification (Fig. 4e). The appearance of PV immunoreactivity was visible in control and post-diceCT brain tissues (Fig. 4f, g), and neuronal somata diameters for experimental treatments did not differ from those of the controls ($t = 0.0585$, $p = 0.956$) (Fig. 4h). In addition, diceCT staining, imaging, and de-staining procedures did not alter cell nuclei counts based on DAPI staining (one-way ANOVA; $F = 1.2565$, $p = 0.325$) (Fig. 4i).

Substantia nigra: DARPP-32 and DAPI staining

We found consistent DARPP-32 (Arlotta et al. 2008) expression in control and post-diceCT brains (Fig. 5b, c). We observed strong staining in cell bodies and of dopaminergic neurons within the SN, and DARPP-32 co-localization with DAPI demonstrated nuclear staining in both tissue treatments (Fig. 5b, c). We found no significant difference in somata diameters between experimental and control brain tissues stained with anti-DARPP-32 ($t = -1.57$, $p = 0.1916$) (Fig. 5d).

Discussion

X-ray imaging of non-mineralized soft tissues is a major challenge to neuroanatomical studies, causing the brain to be intrinsically difficult to document through such means. New tools like X-ray phase-contrast tomography (e.g., Töpperwein et al. 2018) hold great promise to yield 3D histology maps for unstained samples when targeting exceptionally small (~3 mm^3) regions of interest. Contrast agents like iodine enable the visualization of soft neuroanatomical

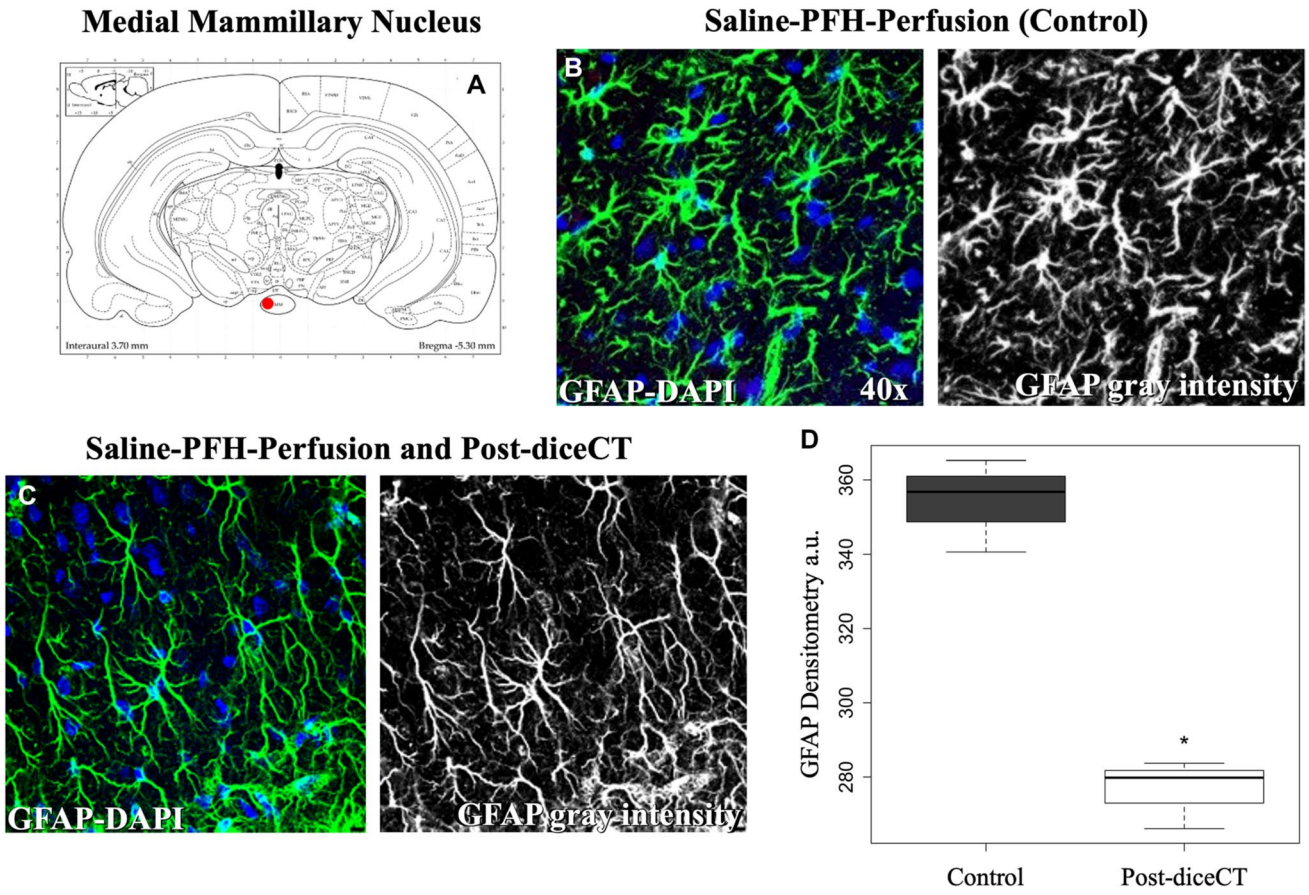

Fig. 3 Medial mammillary (MM) nucleus results. **a** Sampled MM area (red) (Paxinos and Watson 2014). **b**, **c** GFAP-immunoreactive (green) and DAPI-positive (blue) cells in **b** control and **c** and post-diceCT medial mammillary nucleus (scale bar is 20 µm). **d** Mean (±SEM) attenuation units (a.u.) of GFAP-positive cells for control (gray) and post-diceCT (white) MM

features at high resolutions for much larger specimens—in this case entire rat brains (Wong et al. 2013; Lautenschlager et al. 2014; Gignac et al. 2016; Parlanti et al. 2017; Naumann and Olsson 2018). Yet, the resilience of neural tissues to multi-facetted imaging pipelines has not previously been quantified, nor tested explicitly. We used a µCT-based imaging workflow that validates the durability of neuronal proteins, glial cell markers, and nucleic acids after iodine staining. Our results further indicated that many neural phenotypes remain preserved following the iodine staining, imaging, and de-staining process. Further, we superimposed neuroanatomical datasets to visualize structural diversity for the same individual, successfully demonstrating the suitability of brain tissues for a multimodal visualization pipeline, a relevant milestone while working with animal models (Fig. 1). DiceCT, therefore, is not only a low-cost alternative to µMRI for combined cellular and gross-level imaging modalities in organismal and biomedical neuroscience applications but also can be used as a complementary technique that will provide additional information, regarding spatial resolution and tissue organization. Below we discuss the implications of our findings, differentially informative workflow options, factors that may influence the quality of workflow products, and the potential that multiscale, same-sample approaches hold for advancing neuroanatomical research.

Effects of diceCT on histology

Our approach allowed us to survey tissue integrity, which was maintained throughout the diceCT and histology steps of the workflow. DiceCT samples undergo formalin fixation, thermal shifts between refrigerated (4 °C), room (25 °C), and CT-scanner cabinet (> 25 °C) temperatures, weeks in iodine stain without refrigeration, exposure to high-powered X-rays, and de-staining using alternating baths of sodium thiosulfate and de-ionized water (Gignac et al. 2016). Exposure to, and changes between, these environments hold the potential to stress and damage brain tissue beyond its capacity to maintain reactivity to histological stains. We found, instead, that numerous cellular targets remained reactive to histological stains after implementation of diceCT protocols.

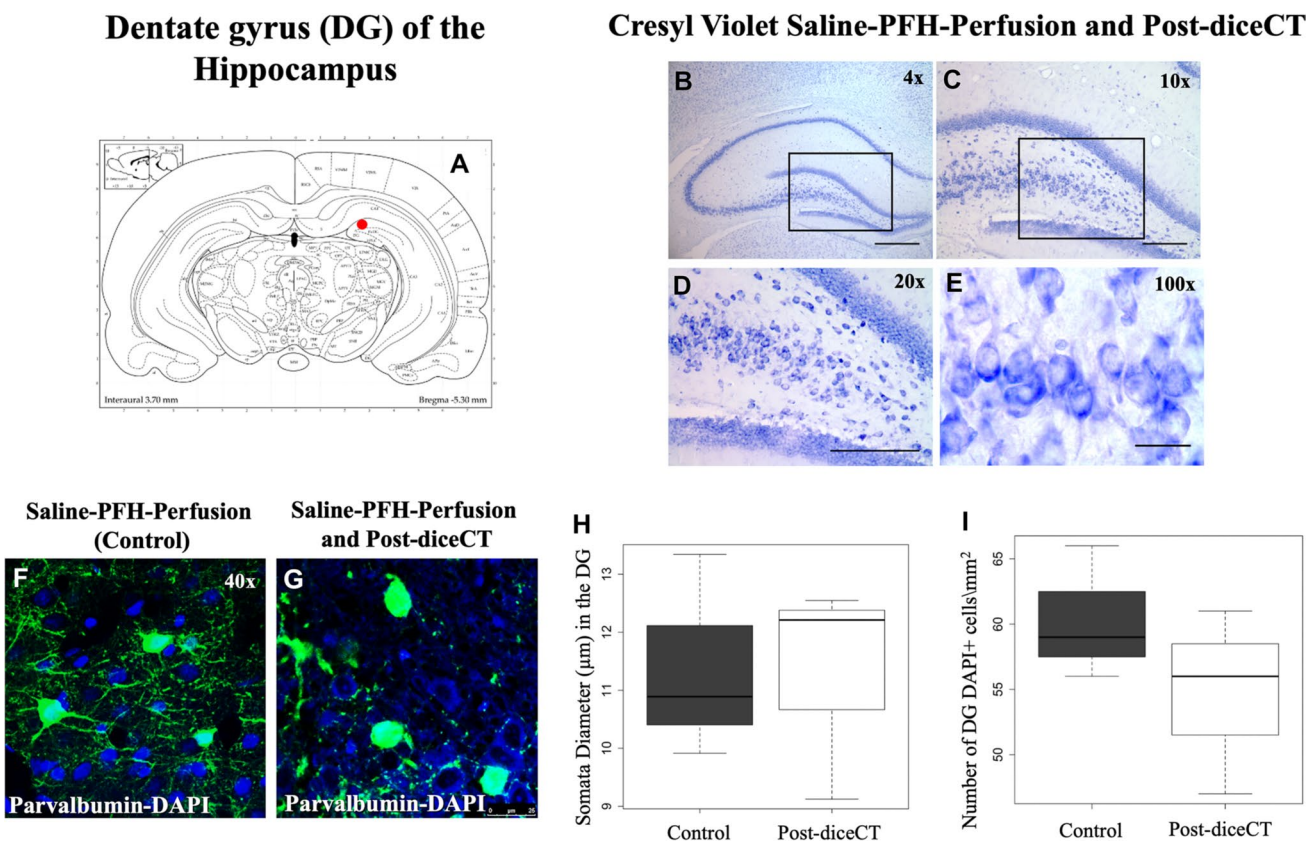

Fig. 4 Dentate gyrus (DG) results. **a** Sampled DG area (red) (Paxinos and Watson 2014). **b**–**e** Cresyl violet-stained DG; insets mark regions magnified (4–100×; scale bars: 600, 250, 60, 25 µm, respectively) in successive panels from **b**–**e**. **f**, **g** PV immunoreactivity (green) and DAPI-positive (blue) cells in **f** control and **g** post-diceCT DG. **h** Mean (±SEM) somata diameter (µm) of DAPI-positive cells for control (gray) and post-diceCT (white) DG. **i** Mean (±SEM) number of PV-immunoreactive cells for control (gray) and post-diceCT (white) mPFC per mm^2

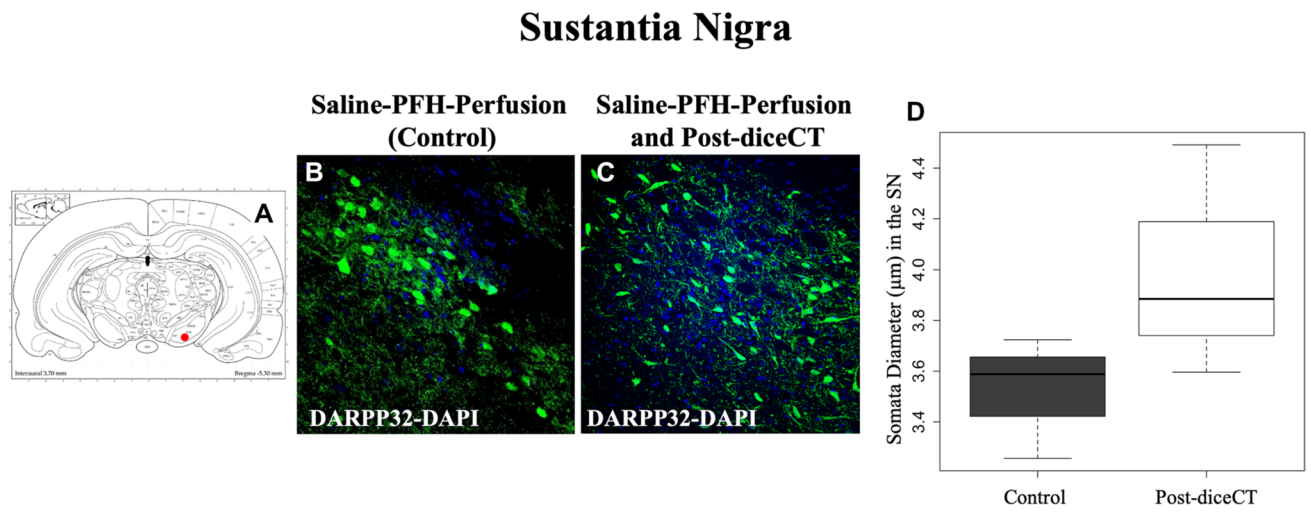

Fig. 5 **a** Sampled area of SN (red) (Paxinos and Watson 2014); **b**, **c** DARPP-32-immunoreactive (green) and DAPI-positive (blue) cells in **b** control and **c** post-diceCT SN. **d** Mean (±SEM) cell diameter (µm) of DAPI-positive cells for control (gray) and post-diceCT (white) SN

Tissue sectioning and targetability, for immunohistochemistry with fluorescence, fluorescent labelling, and standard Nissl-based cytological staining, were maintained after diceCT treatment. This was evidenced by visual and quantitative confirmation of histological labelling following de-staining with sodium thiosulfate. Anti-parvalbumin, which targets calcium-binding proteins and is a major marker for cortical GABAergic interneurons; anti-DARPP-32, which targets D1 dopamine receptors; GFAP, which targets astrocytes; and DAPI and cresyl violet, which target nucleic acids; all showed high subjective histological fidelity in experimental and control tissues. The binding of histological staining agents without color pollution from residual iodine illustrates that iodine was adequately removed from brain tissues by the de-staining protocol. The reversibility of diceCT staining is an important potential differentiator when considering multimodal contrast-enhanced imaging methods (see the survey of contrast agents in Gignac et al. 2016) and a key factor that enables the integrated imaging pipeline presented here. We found it highly valuable to divide the brains into portions for de-staining, parallel to the plane for histological sectioning, because this provided additional surface area for sodium thiosulfate and de-ionized water to diffuse, improving the efficiency of de-staining. By anticipating the plane of histological section, we minimized unnecessary, physical damage to the samples. We recommend similar approaches by other workers undertaking diceCT-histology imaging projects.

Our results show a straightforward pattern of histological reactivity to rat brain tissues and cellular structures after diceCT. However, we found two variables where control and post-diceCT groups differed significantly: GFAP fluorescent signal intensity and mPFC somata diameter. The significant differences between treatments for these variables must be interpreted cautiously, taking into consideration the small sample size used in this study. First, GFAP fluorescent signal intensity deviated from the above-mentioned staining outcomes, demonstrating statistically significant differences in densitometry between control and diceCT treatments (Fig. 3d; Table 1). Specifically, GFAP signal densitometry comparisons quantified differences in labeling expression during astrocyte immunostaining, and signal intensities illustrated that experimental brains showed significantly reduced targetability of GFAP (Table 1). These results may be linked to molecular charge: GFAP expression is modulated in part by lipopolysaccharides (Kang et al. 2019), which are upregulated during astrocyte proliferation. The affinity of triiodide for lipids and carbohydrates may contribute to triiodide-lipopolysaccharide binding that depolymerizes GFAP. Consuming GFAP by this process would reduce available targets for anti-GFAP, also reducing immunostaining intensity. Notably, this phenomenon is likely more pronounced during adolescence, when astrocytogenesis is high (Leal et al. 1997; Akdemir et al. 2020), which characterizes our sample. Thus, the GFAP intensity reduction documented here following diceCT staining may be less pronounced for adult brains. We recommend further evaluation of post-diceCT histology that targets positively charged macromolecules across sample sizes larger than our proof-of-concept. Regardless of the mechanism, reduced anti-GFAP values remained sufficient, even in our adolescent sample, for use as a "phenotyping" marker to distinguish cells as belonging to glial versus neuronal populations (Table 1; Fig. 3). While it remains unclear what accounts for this apparent difference, there could be some unaccounted-for parameters in the histological process that rendered astrocytes more vulnerable to our tissue processing workflow.

The second variable significantly affected by diceCT staining was a reduction in the somata diameter of the mPFC (Fig. 2f; Table 1). Significant somata diameter trends were not observed in other tissues. In the DG, average somata diameter is larger in post-diceCT specimens, although the overall range of variance in post-diceCT somata diameter is slightly lower (Fig. 4h). In SN neurons, both the average and range of somata diameter trended toward larger in post-diceCT specimens (Fig. 5d). Trends in somata sizes may or may not be due strictly to diceCT and sodium thiosulfate immersion. Previous studies identify significant differences in somata sizes due to the use of immersion versus perfusion as the primary method of fixation or other tissue treatment (Lavenex 2008), even when controlling for other procedural factors (Lavenex et al. 2009). Still, other studies have highlighted qualitative differences in histology staining between perfusion- and immersion-fixed central nervous system tissues (e.g., McFadden et al. 2019), and both qualitative and quantitative differences for somatic tissues (e.g., Miller and Meyer 1990). Therefore, we recommend either subjecting all tissues to the same processing methods or using a segregated treatment protocol that does not directly compare somata size between control and post-diceCT protocols (Fig. 6).

The combination of unaffected anti-parvalbumin, anti-DARPP-32, DAPI, and cresyl violet labelling alongside reduced anti-GFAP labelling leads to a broad and preliminary guideline: cellular targets that are eosinophilic appear more likely to be robust to diceCT staining and de-staining protocols. Eosinophilic neural proteins, dopamine receptors, and nucleic acids, including those that we targeted histologically, have net negative charges (i.e., low isoelectric pwpoints; Haiech et al. 1979; Hemmings et al. 1984; Lipfert et al. 2014; O'Dowd et al. 2012). This suggests that they repel the negatively charged triiodide (I_3^-) molecules used in diceCT staining. Triiodide, therefore, may fail to bind these substrates, likely contributing to their preservation for multimodal staining pipelines using diceCT. This suggests that histology, especially immunohistochemistry, following diceCT should target substrates that are basic, have low

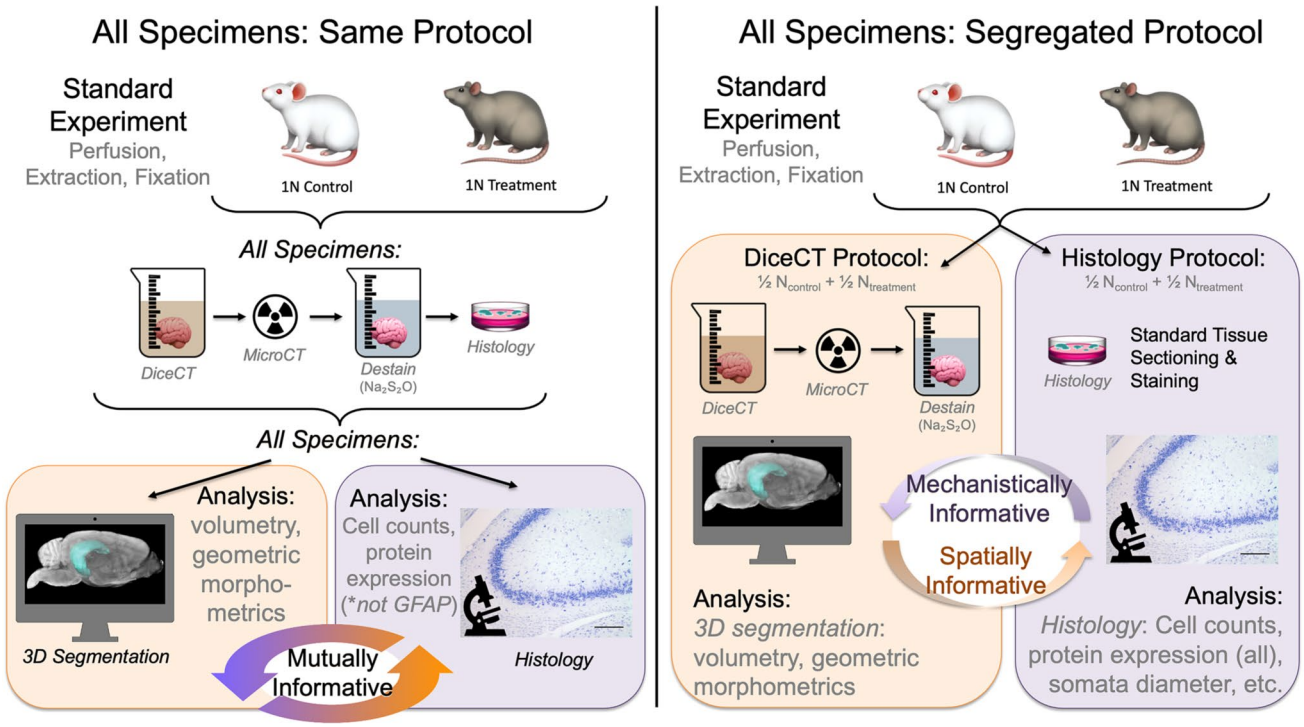

Fig. 6 Prospective diceCT and histology workflows. In the left panel, following an experimental scenario with control and treatment groups, all specimens are treated using the workflow outlined herein [diffusion-based Lugol's iodine staining for contrast-enhancement (diceCT), microCT scanning at high resolution, completely destained with sodium thiosulfate ($Na_2S_2O_2$), and subjected to standard, cresyl violet, or immunohistochemistry histology]. All specimens can then be analyzed using 3D segmentation, including volumetry and geometric morphometrics, as well as histomorphology, in mutually informative contexts. For post-diceCT histology, we recommend including cell counts and protein expression (with the exception of GFAP). When cell counts, protein expression (including GFAP and other acidic molecules), and somata diameter are important analytical targets, we recommend the segregated protocol in the right panel. In the segregated protocol, a proportion of both experimental control and treatment groups are subjected to either the diceCT protocol (note, de-staining is optional) or the histology protocol. Here, 3D segmentation and subsequent analyses can provide whole-region spatial information for histology results, whereas histological results can mechanistically inform interpretation of any observed geometric and volumetric shifts

isoelectric points, or are eosinophilic to produce the best quality results.

We found broadly comparable somata diameter measurements between control and experimental tissues, identifying no significant differences in neuronal size in the DG and SN (Figs. 4h and 5d; Table 1). This finding indicates that soft-tissue distortions, such as volumetric shrinkage that may occur due to iodine staining (Vickerton et al. 2013; Gignac et al. 2016), do not appear to impact neuron size in these brain regions, at least after de-staining and histological preparation. Although somata diameter was affected in the mPFC (see "Discussion" above; Fig. 2f; Table 1), comparable amounts of mPFC- and DG-labeled cells between control and experimental brains indicate that the addition of diceCT to brain-histology protocols does not impact cell densities (Figs. 2e and 4i; Table 1). This suggests that any osmotic water loss due to the high-salt content of the staining agent during the diceCT phase of the pipeline can be reconstituted during the de-staining process with de-ionized water baths. Also, although we did not employ it here for our diceCT-specific methodologies, it is worth noting that PBS is routinely used in the preparation of specimens for neuroimaging (e.g., see "Brain sampling" methods) in part because it does not compromise cytoarchitectures. It may, therefore, be a viable alternative to deionized water for post-stain differentiation and de-staining of diceCT brain and peripheral nervous system samples. Taken together, the diceCT imaging pipeline we articulate here apparently does not alter the cellular configuration of brain tissue samples. Thus, we anticipate that combining diceCT with histological analyses holds enormous promise as a powerful tool for documenting neuroanatomy across spatial scales and in 3D.

Considerations to the preservation of nervous tissues

Nervous tissues must be rapidly fixed with an appropriate concentration and duration of formaldehyde to conduct

histological preparations of the brain (Fox et al. 1985; Hughes et al. 2016b). Consequently, not all approaches to preserving samples will be compatible with our pipeline, and brain preservation methods should be referenced prior to any imaging attempts. For example, although suitable diceCT images of the brain have been achieved from ethanol-fixed specimens (e.g., Prötzel et al. 2018), formaldehyde fixation of nervous tissues is optimal for many steps of histology after diceCT, including tissue sectioning, immunohistochemical staining, and other cell-based stains (Berod et al. 1981). To ensure that the most neuroanatomical data can be gleaned from a single sample, researchers should consider what type of fixative and method of specimen preservation are required to enable continued use of the tissue during downstream investigations. Finally, one potential limitation in our study is that brain tissues can be distorted from shrinkage due to over-staining (Gignac and Kley 2018). There are physical methods and mathematical approaches to address these issues (Weisbecker 2012; Taylor et al. 2020); however, some may be incompatible with the multimodal pipeline described here.

Conclusions

To our knowledge, we are the first to demonstrate that strong nuclear and cytoplasmic labeling of neurons with cresyl violet staining and immunofluorescence after diceCT brain imaging is preserved. The multiscale examination of precious biological samples this enables is an advantageous alternative to single-modality pipelines. Multiscale, same-sample approaches provide greater detail for anatomical regions than is possible using one instrument or method alone. Beyond the conglomerate of staining techniques described here, we also suggest that exploration of labeling strategies for additional basic cellular neurochemical phenotype markers (e.g., tyrosine hydroxylase, choline acetyltransferase) as well as transcription factors (e.g., c-Fos) following diceCT may provide fruitful additions to integrated brain-imaging pipelines. We further recommend µCT-scanning specimens prior to any contrast enhancement to capture skeletal morphology, such as the braincase or whole skull. These more traditional µCT datasets can be combined with whole-brain diceCT and region-of-interest histology for use in studying structural anatomy across orders of magnitude in spatial scale that achieves ample coverage of external morphology and internal anatomy resulting in a cell-to-skull hierarchy of data. Whether harnessed for model organisms (Cole 1944; Preuss 2000; Keifer and Summers 2016; Khan et al. 2018), translational research (Bonnier et al. 2014; Vazquez-Sanroman et al. 2017; Kim et al. 2019), or comparative neuroanatomical studies (Yartsev 2017), pipelines such as these hold great promise for unlocking data that can be unintentionally trapped by single-method preparations, especially those that do not adequately preserve deep internal soft tissues, such as the brain. To unlock general principles of nervous system organization across the tree of life (Butler and Hodos 2005; Manger et al. 2008; Carlson 2012; Striedter, 2014; Brenowitz and Zakon 2015; Russell et al. 2017), highly integrative approaches, as we have demonstrated here, are key (Schwenk et al. 2009; Dowling et al. 2010; Vogelstein et al. 2014).

Supplementary Information The online version contains supplementary material available at https://doi.org/10.1007/s00429-021-02316-6.

Acknowledgements We owe special thanks to all UTEP Systems Neuroscience Laboratory members, especially Daniel F. Hughes and Arshad M. Khan, for their valuable comments and feedback. Also, we thank Dr. Daniela Carulli from Neuroscience Otto Lenghi center in University of Turin for the valuable insight in image analysis. We thank Morgan H. Chase and the AMNH Microscopy and Imaging Facility for assistance.

Funding PMG was supported by NSF (1450850, 1457180, and 1754659) and the American Association for Anatomy. DVS, HDO, and PMG were supported by the OSU-CHS department of Anatomy and Cell Biology. DVS and HDO were also supported by the OSU-CHS Office of the Vice President for Research. JS was supported by pre-doctoral fellowship from the National Mexican Council of Education (CONACyT).

Declarations

Conflict of interest The authors declare no conflicts of interest.

Research involving human participants and/or animals All surgical and testing procedures were approved by the Oklahoma State University Institutional Animal Care and Use Committee and conformed to NIH guidelines.

References

Akdemir ES, Huang AY-S, Deneen B (2020) Astrocytogenesis: where, when, and how [version 1; peer review: 2 approved]. F1000Research 9:233. https://doi.org/10.12688/f1000research.22405.1 (**F1000 Faculty Rev**)

Alonso JR, Arevalo R, Brinon JG, Lara J, Weruaga E, Aijon J (1992) Parvalbumin immunoreactive neurons and fibres in the teleost cerebellum. Anatomy and embryology 185(4):355–361. https://doi.org/10.1007/BF00188547

Anderson R, Maga AM (2015) A novel procedure for rapid imaging of adult mouse brains with microCT using iodine-based contrast. PLoS ONE 10:e0142974. https://doi.org/10.1371/journal.pone.0142974

Arlotta P, Molyneaux BJ, Jabaudon D, Yoshida Y, Macklis JD (2008) Ctip2 controls the differentiation of medium spiny neurons and the establishment of the cellular architecture of the striatum. J Neurosci 28(3):622–632. https://doi.org/10.1523/JNEUROSCI.2986-07.2008

Basser PJ, Mattiello J, LeBihan D (1994) Estimation of the effective self-diffusion tensor form the NMR spin echo. J Mag Reson B 103:247–254. https://doi.org/10.1006/jmrb.1994.1037

Berod A, Hartman BK, Pujol JF (1981) Importance of fixation in immunohistochemistry: use of formaldehyde solutions at variable pH for the localization of tyrosine hydroxylase. J Histochem Cytochem 29:844–850. https://doi.org/10.1177/29.7.6167611

Bonnier G, Roche A, Romascano D et al (2014) Advanced MRI unravels the nature of tissue alterations in early multiple sclerosis. Ann Clin Transl Neurol 1(6):423–432. https://doi.org/10.1002/acn3.68

Bowler K, Tirri R (1974) The temperature characteristics of synaptic membrane ATPases from immature and adult rat brain. J Neurochem 23:611–613. https://doi.org/10.1111/j.1471-4159.1974.tb06068.x

Brenowitz EA, Zakon HH (2015) Emerging from the bottleneck: benefits of the comparative approach to modern neuroscience. Trends Neurosci 38:273–278. https://doi.org/10.1016/j.tins.2015.02.008

Burger FJ, Fuhrman FA (1964) Evidence of injury by heat in mammalian tissues. Am J Physiol 206:1057–1064. https://doi.org/10.1152/ajplegacy.1964.206.5.1057

Burnett TL, McDonald SA, Gholinia A et al (2014) Correlative tomography. Sci Rep 4:4711. https://doi.org/10.1038/srep04711

Butler AB, Hodos W (2005) Comparative vertebrate neuroanatomy: evolution and adaptation. John Wiley & Sons (**ISBN: 978-0-471-73384-3**)

Caplan J, Niethammer M, Taylor RM II, Czymmek KJ (2011) The power of correlative microscopy: multimodal, multi-scale, multi-dimensional. Curr Opin Struct Biol 21:686–693. https://doi.org/10.1016/j.sbi.2011.06.010

Carlson BA (2012) Diversity matters: diversity matters: the importance of comparative studies and the potential for synergy between neuroscience and evolutionary biology. Arch Neurol 69:987–993. https://doi.org/10.1001/archneurol.2012.77

Carpenter A, Jones T, Lamprecht M, Clarke C, Kang I, Friman O, Guertin D, Chang J, Lindquist R, Moffat J, Golland P, Sabatini D (2006) CellProfiler: image analysis software for identifying and quantifying cell phenotypes. Genome Biol 7(10):R100.1-R111. https://doi.org/10.1186/gb-2006-7-10-r100

Chen Y, Lin G, Chen Y, Fok A, Slack JM (2012) Micro-computed tomography for visualizing limb skeletal regeneration in young *Xenopus* frogs. Anat Rec 295:1562–1565. https://doi.org/10.1002/ar.22496

Cole FJ (1944) A history of comparative anatomy from Aristotle to the eighteenth century. MacMillan & Co (**ISBN: 9780486602240**)

Damadian R, Minkoff L, Goldsmith M, Stanford M, Koutcher J (1976) Field focusing nuclear magnetic resonance (FONAR): visualization of a tumor in a live animal. Science 194:1430–1432. https://doi.org/10.1126/science.1006309

de Crespigny A, Bou-Reslan H, Nishimura MC, Phillips H, Carano RA, D'Arceuil HE (2008) 3D micro-CT imaging of the postmortem brain. J Neurosci Methods 171:207–213. https://doi.org/10.1016/j.jneumeth.2008.03.006

DeCoster MA (2007) The nuclear area factor (NAF): a measure for cell apoptosis using microscopy and image analysis. In: Méndez-Vila A, Diaz J (eds) Modern research and educational topics in microscopoy. Formatex, pp 378–384

Ding SL, Royall JJ, Sunkin SM et al (2016) Comprehensive cellular-resolution atlas of the adult human brain. J Comp Neurol 524:3127–3481. https://doi.org/10.1002/cne.24080

Dodd SJ, Williams M, Suhan JP, Williams DS, Koretsky AP, Ho C (1999) Detection of single mammalian cells by high-resolution magnetic resonance imaging. Biophys J 76:103–109. https://doi.org/10.1016/S0006-3495(99)77182-1

Dowling AP, Bauchan GR, Ochoa R, Beard JJ (2010) Scanning electron microscopy vouchers and genomic data from an individual specimen: maximizing the utility of delicate and rare specimens. Acarologia 50:479–485. https://doi.org/10.1051/acarologia/20101983

Feldkamp LA, Goldstein SA, Parfitt AM, Jesion G, Kleerekoper M (1989) The direct examination of three-dimensional bone architecture in vitro by computed tomography. J Bone Miner Res 4:3–11. https://doi.org/10.1002/jbmr.5650040103

Fox J, Weisberg S (2019) An R companion to applied regression, 3rd edn. Sage, Thousand Oaks

Fox CH, Johnson FB, Whiting J, Roller PP (1985) Formaldehyde fixation. J Histochem Cytochem 33:845–853. https://doi.org/10.1177/33.8.3894502

Gabbott PLA, Dickie BGM, Vaid RR, Headlam AJN, Bacon SJ (1997) Local-circuit neurons in the medial prefrontal cortex (areas 25, 32 and 24b) in the rat: morphology and quantitative distribution. J Comp Neurol 377:465–499. https://doi.org/10.1002/(SICI)1096-9861(19970127)377:4%3c465::AID-CNE1%3e3.0.CO;2-0

Gignac PM, Kley NJ (2018) The utility of diceCT imaging for high-throughput comparative neuroanatomical studies. Brain Behav Evol 91:180–190. https://doi.org/10.1159/000485476

Gignac PM, Kley NJ, Clarke JA (2016) Diffusible iodine-based contrast-enhanced computed tomography (diceCT): an emerging tool for rapid, high-resolution, 3-D imaging of metazoan soft tissues. J Anat 228:889–909. https://doi.org/10.1111/joa.12449

Gignac PM, Green TL, Oehler D, Malatos J, Hollinger C, Pare JA (2021) Diffusible iodine-based contrast-enhanced computed tomography as a necropsy aid in veterinary medicine and wildlife biology: a case study evaluation respiratory disease in *Macrocephalon maleo*. J Zoo Wildl Med 52:406–412. https://doi.org/10.1638/2020-0086

Gold S, Cahani M, Sohmer H, Horowitz M, Shahar A (1985) Effects of body temperature elevation on auditory nerve-brain-stem evoked responses and EEGs in rats. Electroencephalogr Clin Neurophysiol 60:146–153. https://doi.org/10.1016/0013-4694(85)90021-5

Gwóźdź B, Krauze M, Dyduch A (1970) Investigations on oxidative phosphorylation in the brain tissue of animals subjected to high temperature. Acta Physiol Pol 21:239–245 (**PMID: 5420887**)

Gwóźdź B, Dyduch A, Grzybek H, Panz B (1978) Structural changes in brain mitochondria of mice subjected to hyperthermia. Exp Pathol 15:124–126. https://doi.org/10.1016/S0014-4908(78)80077-5

Haiech J, Derancourt J, Pechère J-F, Demaille JG (1979) Magnesium and calcium binding to parvalbumins: evidence for differences between parvalbumins and an explanation of their relaxing function. Biochemistry 19:2752–2758. https://doi.org/10.1021/bi00580a010

Hawkins RA, Hoh C, Glaspy J et al (1992) The role of positron emission tomography in oncology and other whole-body applications. Semin Nucl Med 22:268–284. https://doi.org/10.1016/S0001-2998(05)80121-7

Heimel P, Swiadek NV, Slezak P, Kerbl M, Schneider C, Nürnberger S, Redl H, Teuschle AH, Hercher D (2019) Iodine-enhanced micro-CT imaging of soft tissue on the example of peripheral nerve regeneration. Contrast Media Mol Imaging 7483745:1–15. https://doi.org/10.1155/2019/7483745

Helmy IM, Azim AMA (2012) Efficacy of ImageJ in the assessment of apoptosis. Diagn Pathol 7:15–20. https://doi.org/10.1186/1746-1596-7-15

Hemmings HC Jr, Greengard P (1986) DARPP-32, a dopamine-regulated phosphoprotein. Prog Brain Res 69:149–159. https://doi.org/10.1016/S0079-6123(08)61056-0

Hemmings HC Jr, Nairn AC, Aswad DW, Greengard P (1984) DARPP-32, a dopamine- and adenosine 3′:5′-monophosphate-regulated phosphoprotein enriched in dopamine-innervated brain regions. II. Purification and characterization of the phosphoprotein from bovine caudate nucleus. J Neurosci 4:99–110. https://doi.org/10.1523/JNEUROSCI.04-01-00099.1984

Herdina AN, Plenk H, Benda P (2015) Correlative 3D-imaging of *Pipistrellus* penis micromorphology: validating quantitative microCT images with undecalcified serial ground section histomorphology. J Morphol 276:695–706. https://doi.org/10.1002/jmor.20372

Hinshaw WS, Bottomley PA, Holland GN (1977) Radiographic thin-section image of the human wrist by nuclear magnetic resonance. Nature 270:722–723. https://doi.org/10.1038/270722a0

Hopkins TM, Heilman AM, Liggett JA, LaSance K, Little KJ, Hom DB, Minteer DM, Marra KG, Pixley SK (2015) Combining micro-computed tomography with histology to analyze biomedical implants for peripheral nerve repair. J Neurosci Methods 255:122–130. https://doi.org/10.1016/j.jneumeth.2015.08.016

Hounsfield GN (1977) The E.M.I scanner. Proc R Soc Lond B 195:281–289. https://doi.org/10.1098/rspb.1977.0008

Hughes DF, Gignac PM, Greenbaum E, Khan AM (2016a) Documenting brain diversity in field-caught lizards, from skull to cell: initial development of a processing pipeline for top down, multi-scale structural analyses of a single brain by integrating specialized microcomputed tomography (diceCT). In: Nissl-based cytoarchitectonics, and immunohistochemistry. Program No. 778.02. Neuroscience meeting planner

Hughes DF, Walker EM, Gignac PM et al (2016b) Rescuing perishable neuroanatomical information from a threatened biodiversity hotspot: remote field methods for brain tissue preservation validated by cytoarchitectonic analysis, immunohistochemistry, and x-ray microcomputed tomography. PLoS ONE 11:e0155824. https://doi.org/10.1371/journal.pone.0155824

Jackson JA, Langham WH (1968) Whole-body NMR spectrometer. Rev Sci Instrum 39(510–5):13. https://doi.org/10.1063/1.1683420

Jeffery NS, Stephenson RS, Gallagher JA, Jarvis JC, Cox PG (2011) Micro-computed tomography with iodine staining resolves the arrangement of muscle fibres. J Biomech 44:189–192. https://doi.org/10.1016/j.jbiomech.2010.08.027

Jellison BJ, Field AS, Medow J et al (2004) Diffusion tensor imaging of cerebral white matter: a pictorial review of physics, fiber tract anatomy, and tumor imaging patterns. Am J Neuroradiol 25:356–369 (**PMID: 15037456**)

Jones T, Townsend D (2017) History and future technical innovation in positron emission tomography. J Med Imaging 4:011013. https://doi.org/10.1117/1.JMI.4.1.011013

Kang J-B, Park D-J, Shah M-A, Kim M-O, Koh P-O (2019) Lipopolysaccharide induces neuroglia activation and NF-kB activation in cerebral cortex of adult mice. Lab Anim Res 35:19. https://doi.org/10.1186/s42826-019-0018-9

Karreman MA, Mercier L, Schieber NL et al (2016) Fast and precise targeting of single tumor cells in vivo by multimodal correlative microscopy. J Cell Sci 129:444–456. https://doi.org/10.1242/jcs.181842

Keifer J, Summers CH (2016) Putting the "biology" back into "neurobiology": the strength of diversity in animal model systems for neuroscience research. Front Syst Neurosci 10:69. https://doi.org/10.3389/fnsys.2016.00069

Khan AM, Grant AH, Martinez A et al (2018) Mapping molecular datasets back to the brain regions they are extracted from: remembering the native countries of hypothalamic expatriates and refugees. Adv Neurobiol 21:101–193. https://doi.org/10.1007/978-3-319-94593-4_6

Kim C-B, Park S-J, Jeong J-C (2019) Construction of 3D-rendering imaging of an ischemic rat brain model using the planar FMMD technique. Sci Rep 9:19050. https://doi.org/10.1038/s41598-019-55585-x

Kondo H, Fukuda H, Ono H et al (2001) Sodium thiosulfate solution spray for relief of irritation caused by Lugol's stain in chromoendoscopy. Gastrointest Endosc 53:199–202. https://doi.org/10.1067/mge.2001.110730

Kubota Y, Hattori R, Yui Y (1994) Three distinct subpopulations of GABAergic neurons in rat frontal agranular cortex. Brain Res 649:159–173. https://doi.org/10.1016/0006-8993(94)91060-X

Laine RF, Tosheva KL, Gustafsson N, Gray RDM, Almada P, Albrecht D, Risa GT, Hurtig F, Lindås AC, Baum B, Mercer J, Leterrier C, Pereira PM, Culley S, Henriques R (2019) NanoJ: a high-performance open-source super-resolution microscopy toolbox. J Phys D Appl Phys 52(16):163001. https://doi.org/10.1088/1361-6463/ab0261

Lautenschlager S, Bright JA, Rayfield EJ (2014) Digital dissection-using contrast-enhanced computed tomography scanning to elucidate hard-and soft-tissue anatomy in the common buzzard *Buteo buteo*. J Anat 224:412–431. https://doi.org/10.1111/joa.12153

Lauterbur PC (1974) Magnetic resonance zeugmatography. Pure Appl Chem 40:119–157. https://doi.org/10.1351/pac197440010149

Lavenex P (2008) Neuroanatomy methods in humans and animals. In: Squire LR (ed) New encyclopedia of neuroscience. Elsevier, Amsterdam. https://doi.org/10.1016/B978-008045046-9.00325-9

Lavenex P, Lavenex PB, Bennett JL, Amaral DG (2009) Postmortem changes in the neuroanatomical characteristics of the primate brain: the hippocampal formation. J Comp Neurol 512(1):27–51. https://doi.org/10.1002/cne.21906

Leal RB, Gonçalves CA, Rodnight R (1997) Calcium-dependent phosphorylation of glial fibrillary acid protein (GFAP) in the rat hippocampus: a comparison of the kinase/phosphatase balance in immature and mature slices using tryptic phosphopeptide mapping. Dev Brain Res 105:1–10. https://doi.org/10.1016/s0165-3806(97)00113-2

Lipfert J, Doniach S, Das R, Herschlag D (2014) Understanding nucleic acid-ion interactions. Annu Rev Biochem 83:813–841. https://doi.org/10.1146/annurev-biochem-060409-092720

Manger P, Cort J, Ebrahim N, Goodman A, Henning J, Karolia M, Rodrigues SL, Strkalj G (2008) Is 21st century neuroscience too focused on the rat/mouse model of brain function and dysfunction? Front Neuroanat 2:5. https://doi.org/10.3389/neuro.05.005.2008

McDonald LW, Hayes TL (1969) Correlation of scanning electron microscope and light microscope images of individual cells in human blood and blood clots. Exp Mol Pathol 10:186–198

McFadden WC, Walsh H, Richter F, Soudant C, Bryce CH, Hof PR, Fowkes M, Crary JF, McKenzie AT (2019) Perfusion fixation in brain banking: a systematic review. Acta Neuropathol Commun 7:146. https://doi.org/10.1186/s40478-019-0799-y

Millan N, Murdock LL, Bleier R, Siegel FL (1979) Effects of the acute hyperthermia on polyribosomes, in vivo protein synthesis and ornithine decarboxylase activity in the neonatal rat brain. J Neurochem 32:311–317

Miller PL, Meyer TW (1990) Effects of tissue preparation on glomerular volume and capillary structure in the rat. Lab Invest 63(6):862–866

Morales AG, Stempinski ES, Xiao X, Patel A, Panna A, Olivier KN, McShane PJ, Robinson C, George AJ, Donahue DR, Chen P (2016) Micro-CT scouting for transmission electron microscopy of human tissue specimens. J Microsc 263:113–117

Muehllehner G, Buchin MP, Dudek JH (1976) Performance parameters of a positron imaging camera. IEEE Trans Nucl Sci 23:528–537. https://doi.org/10.1109/TNS.1976.4328300

Nair-Roberts RG, Chatelain-Badie SD, Benson E, White-Cooper H, Bolam JP, Ungless MA (2008) Stereological estimates of dopaminergic, GABAergic and glutamatergic neurons in the ventral tegmental area, substantia nigra and retrorubral field in the rat. Neuroscience 152(4):1024–1031. https://doi.org/10.1016/j.neuroscience.2008.01.046

Nasrullah Q, Renfree MB, Evans AR (2018) Three-dimensional mammalian tooth development using diceCT. Arch Oral Biol 85:183–191. https://doi.org/10.1016/j.archoralbio.2017.10.018

Naumann A, Olsson L (2018) Three-dimensional reconstruction of the cranial and anterior spinal nerves in early tadpoles of *Xenopus laevis* (Pipidae, Anura). J Comp Neurol 526:836–857

O'Dowd BF, Ji X, Nguyen T, George SR (2012) Two amino acids in each of D_1 and D_2 dopamine receptor cytoplasmic regions are involved in D1–D2 heteromer formation. Biochem Biophys Res Commun 417(1):23–28. https://doi.org/10.1016/j.bbrc.2011.11.027

Parlanti P, Cappello V, Brun F, Tromba G, Rigolio R, Tonazzini I, Cecchini M, Piazza V, Gemmi M (2017) Size and specimen-dependent strategy for X-ray micro-CT and TEM correlative analysis of nervous system samples. Sci Rep 7:2858

Paxinos G, Watson C (2014) The rat brain in stereotaxic coordinates, 7th edn. Elsevier (**ISBN: 9780123919496**)

Pelc NJ (2014) Recent and future directions in CT imaging. Ann Biomed Eng 42(2):260–268. https://doi.org/10.1007/s10439-014-0974-z

Phelps ME, Hoffman EJ, Mullani NA, Higgins CS, Pogossian MMT (1976) Design considerations for a positron emission transaxial tomograph (PETT III). IEEE Trans Nucl Sci 23:516–522. https://doi.org/10.1109/TNS.1976.4328298

Preuss TM (2000) Taking the measure of diversity: comparative alternatives to the model-animal paradigm in cortical neuroscience. Brain Behav Evol 55:287–299

Prötzel D, Vences M, Hawlitschek O, Scherz MD, Ratsoavina FM, Glaw F (2018) Endangered beauties: micro-CT cranial osteology, molecular genetics and external morphology reveal three new species of chameleons in the *Calumma boettgeri* complex (Squamata: Chamaeleonidae). Zool J Linn Soc 184:471–498

Rahati M, Nozari M, Eslami H, Shabani M, Basiri M (2016) Effects of enriched environment on alterations in the prefrontal cortex GFAP- and S100B-immunopositive astrocytes and behavioral deficits in MK-801-treated rats. Neuroscience 326:105–116. https://doi.org/10.1016/j.neuroscience.2016.03.065

Rekha J, Chakravarthy S, Veena LR, Kalai VP, Choudhury R, Halahalli HN, Alladi PA, Dhanushkodi A, Nirmala M, Swamilingiah GM, Agrahari M, Raju TR, Panicker MM, Kutty BM (2009) Transplantation of hippocampal cell lines restore spatial learning in rats with ventral subicular lesions. Behav Neurosci 123(6):1197–1217. https://doi.org/10.1037/a0017655

Rüegsegger P, Koller B, Müller R (1996) A microtomographic system for the nondestructive evaluation of bone architecture. Calcif Tissue Int 58:24–29. https://doi.org/10.1007/bf02509542

Russell JJ, Theriot JA, Sood P, Marshall WF, Landweber LF, Fritz-Laylin L, Polka JK, Oliferenko S, Gerbich T, Gladfelter A, Umen J (2017) Non-model model organisms. BMC Biol 15:55

Schwenk K, Padilla DK, Bakken GS, Full RJ (2009) Grand challenges in organismal biology. Integr Comp Biol 49:7–14. https://doi.org/10.1093/icb/icp034

Sengle G, Tufa SF, Sakai LY, Zulliger MA, Keene DR (2013) A correlative method for imaging identical regions of samples by micro-CT, light microscopy, and electron microscopy: imaging adipose tissue in a model system. J Histochem Cytochem 61:263–271

Senter-Zapata M, Patel K, Bautista PA, Griffin M, Michaelson J, Yagi Y (2016) The role of micro-CT in 3D histology imaging. Pathobiology 83:140–157. https://doi.org/10.1159/000442387

Shakhashiri B (1983) Chemical demonstrations: a handbook for teachers of chemistry, vol 3. University of Wisconsin Press, Madison

Shami GJ, Cheng D, Braet F (2017) Combined multidimensional microscopy as a histopathology imaging tool. J Cell Physiol 232:249–256

Smith BR, Linney E, Huff DS, Johnson GA (1996) Magnetic resonance microscopy of embryos. Comput Med Imaging Graph 20:483–490. https://doi.org/10.1016/S0895-6111(96)00046-8

Striedter GF et al (2014) NSF workshop report: discovering general principles of nervous system organization by comparing brain maps across species. J Comp Neurol 522:1445–1453

Swanson LW (2018) Brain maps 4.0—structure of the rat brain: an open access atlas with global nervous system nomenclature ontology and flatmaps. J Comp Neurol 526:935–943

Taylor MS, O'Brien HD, Gignac PM (2020). Shrinkage after swimming in iodine? Evaluating the use of hydrogel stabilization for reinforcing nervous tissues before iodine diffusion. In: Society for integrative and comparative biology abstracts, 122-2

Ter-Pogossian MM, Phelps ME, Hoffman EJ, Mullani NA (1975) A positron-emission transaxial tomography for nuclear imaging (PETT). Radiology 114:89–98. https://doi.org/10.1148/114.1.89

Töpperwein M, van der Meer F, Stadelmann C, Salditt T (2018) Three-dimensional virtual histology of human cerebellum by X-ray phase-contrast tomography. Proc Natl Acad Sci 115:6940–6945. https://doi.org/10.1073/pnas.1801678115

Trevorrow V, Fashena G (1935) The determination of iodine in biological material. J Biol Chem 110:29–38

Vazquez-Sanroman DB, Monje RD, Bardo MT (2017) Nicotine self-administration remodels perineuronal nets in ventral tegmental area and orbitofrontal cortex in adult male rats. Addict Biol 22:1743–1755

Vickerton P, Jarvis J, Jeffery N (2013) Concentration-dependent specimen shrinkage in iodine-enhanced microCT. J Anat 223:185–193. https://doi.org/10.1111/joa.12068

Vogelstein JT, Park Y, Ohyama T, Kerr RA, Truman JW, Priebe CE, Zlatic M (2014) Discovery of brainwide neural-behavioral maps via multiscale unsupervised structure learning. Science 344:386–392

Voie AH, Burns DH, Spelman FA (1993) Orthogonal-plane fluorescence optical sectioning: three-dimensional imaging of macroscope biological specimens. J Microsc 170:229–236. https://doi.org/10.1111/j.1365-2818.1993.tb03346.x

Weisbecker V (2012) Distortion in formalin-fixed brains: using geometric morphometrics to quantify the worst-case scenario in mice. Brain Struct Funct 217:677–685

Wong MD, Spring S, Henkelman RM (2013) Structural stabilization of tissue for embryo phenotyping using micro-CT with iodine staining. PLoS ONE 8:e84321

Yartsev MM (2017) The emperor's new wardrobe: rebalancing diversity of animal models in neuroscience research. Science 358:466–469